Atmos. Meas. Tech. Discuss., doi:10.5194/amt-2017-62, 2017
Manuscript under review for journal Atmos. Meas. Tech.
Discussion started: 14 March 2017

Atmospheric Measurement Techniques Discussions

Intercomparison of Open-Path Trace Gas Measurements with Two Dual Frequency Comb Spectrometers

Eleanor M. Waxman[1], Kevin C. Cossel[1], Gar-Wing Truong[1], Fabrizio R. Giorgetta[1], William C. Swann,[1]
Sean Coburn[2], Robert J. Wright[2], Gregory B. Rieker[2], Ian Coddington,[1] and Nathan R. Newbury[1]
[1]Physical Measurement Laboratory, National Institute of Standards and Technology, 325 Broadway, Boulder, CO 80305
[2]Precision Laser Diagnostics Laboratory, University of Colorado Boulder, Boulder, CO 80309
Correspondence to: Eleanor Waxman
(eleanor.waxman@nist.gov)

Abstract
We present the first quantitative intercomparison between two open-path dual comb spectroscopy (DCS) instruments which were operated across adjacent 2-km open-air paths over a two-week period. We used DCS to measure the atmospheric absorption spectrum in the near infrared from 6021 to 6388 cm^{-1} (1565 to 1661 nm), corresponding to a 367 cm^{-1} bandwidth, at 0.0067 cm^{-1} sample spacing. The measured absorption spectra agree with each other to within 5×10^{-4} without any external calibration of either instrument. The absorption spectra are fit to retrieve concentrations for carbon dioxide (CO_2), methane (CH_4), water (H_2O), and deuterated water (HDO). The retrieved dry mole fractions agree to 0.14% (0.57 ppm) for CO_2, 0.35% (7 ppb) for CH_4, and 0.40% (36 ppm) for H_2O over the two-week measurement campaign, which included 23 °C outdoor temperature variations and periods of strong atmospheric turbulence. This agreement is at least an order of magnitude better than conventional active-source open-path instrument intercomparisons and is particularly relevant to future regional flux measurements as it allows accurate comparisons of open-path DCS data across locations and time. We additionally compare the open-path DCS retrievals to a WMO-calibrated cavity ringdown point sensor located along the path with good agreement. Short-term and long-term differences between the two systems are attributed, respectively, to spatial sampling discrepancies and to inaccuracies in the current spectral database used to fit the DCS data. Finally, the two-week measurement campaign yields diurnal cycles of CO_2 and CH_4 that are consistent with the presence of local sources of CO_2 and absence of local sources of CH_4.

1. Introduction

Quantitative determination of greenhouse gas fluxes over a variety of temporal and spatial scales is necessary for characterizing source strength and intermittency and for future emissions monitoring, reporting, and verification. To this end, techniques exist to measure greenhouse gas concentrations on a variety of length scales, each of which has advantages and disadvantages. Point sensors provide valuable information about local sources, but their use for continuous regional measurements on sampling towers is complicated by local wind patterns, local sources, and mixing within the planetary boundary layer (PBL), especially at night (Lauvaux et al., 2008; Ciais et al., 2010; Lauvaux et al., 2012). Similarly, total-column measurements are particularly useful for sub-continental to global scale measurements; however they are sensitive to atmospheric transport errors within the PBL (Lauvaux and Davis, 2014), are affected by clouds and aerosols, are primarily limited to daytime measurements, and lack either the revisit rates or mobility for regional flux measurements. Horizontal integrated path measurements are complementary to point sensors and satellites: they cover spatial scales from 1-10s of kilometers and provide measurements on the second to minute time scales with portable instruments and are thus appropriate for regional studies. Active-source open-path sensors such as open-path Fourier Transform Infrared spectroscopy (FTIR), differential optical absorption

Atmos. Meas. Tech. Discuss., doi:10.5194/amt-2017-62, 2017
Manuscript under review for journal Atmos. Meas. Tech.
Discussion started: 14 March 2017

Atmospheric Measurement Techniques Discussions

spectroscopy (DOAS), differential LIDAR (DIAL), or tunable diode laser absorption spectroscopy (TDLAS) are often used for these measurements and can retrieve path-averaged concentrations but typically with 10% or greater uncertainties (EPA Handbook, and references therein). Recently, open-path dual-comb spectroscopy (DCS) has emerged as a new technique that could potentially provide precise, accurate continuous regional measurements of the mole fractions of CO_2, CH_4, H_2O, and HDO over kilometer-scale open paths (Rieker et al., 2014), thereby providing a new open-path sensing capability that falls between point sensing and total-column measurements.

Here we demonstrate that open-path DCS can indeed yield dry mole fractions over open-air paths with a high level of intercomparibility, over long periods of time, and with sufficient precision to track variations in the ambient levels from local sources and sinks. Two completely independent open-path DCS instruments are operated over neighboring open-air paths during a two-week measurement campaign. Although both DCS instruments use fully stabilized frequency combs, they are portable (Truong et al., 2016) and are operated nearly continuously during both day and night through laboratory temperature variations from 17 to 25°C, strong atmospheric turbulence, and outdoor air temperature variations from 4.6 to 28.9°C. The retrieved dry mole fractions for the two DCS instruments agree to better than 0.57 ppm[1] (0.14 %) for CO_2 and 7.0 ppb (0.37 %) for CH_4. This agreement is achieved without any "bias correction" or calibration of either instrument for absolute wavelength or for absolute concentration. Instead, it is a direct consequence of the negligible instrument lineshape and precise frequency calibration of the DCS instruments, which leads to measured atmospheric absorption spectra that are identical to below 10^{-3} (limited by the instrument noise level). The measured path-averaged CO_2 precision over a 2-km path is 0.90 ppm in 30 seconds, improving to 0.24 ppm in 5 minutes. For CH_4, the precision is 9.6 ppb in 30 seconds, improving to 2.1 ppb in 5 minutes. We also compare the DCS retrievals to a WMO-calibrated, cavity ringdown point sensor located near the path. The agreement is within 3.4 ppm and 17 ppb for CO_2 and CH_4 respectively, limited by differences in the sampling volume and by the spectral database used to analyze the DCS transmission spectra.

Similar intercomparison measurements between conventional active, open-path sensors are rare but have shown agreement of typically 1-20% (Thoma et al., 2005; Hak et al., 2005; Smith et al., 2011; Shao et al., 2013; Conde et al., 2014; Reiche et al., 2014; Thalman et al., 2015). Here, we find agreement between two DCS instruments that is an order of magnitude better and is comparable to that achieved with highly-calibrated, state-of-the-art, solar-looking FTIRs that retrieve vertical column measurements (Messerschmidt et al., 2011; Frey et al., 2015; Hedelius et al., 2016); however, open-path DCS does not require instrument-specific calibrations (e.g. of the instrument line shape) and provides a very different capability by retrieving the dry mole fractions across regional, kilometer-scale paths over day and night in a mobile platform. Moreover, as the agreement between open-path DCS instruments is below the level of natural background fluctuations, future measurements can facilitate accurate inverse modeling to identify sources and sinks of carbon emission over regions. As an initial demonstration, we discuss the observed diurnal variations from this two-week measurement campaign in the final section of the paper.

2 Technique

2.1 Overview

DCS is based on a frequency comb laser source, which is a pulsed laser that outputs a spectrum consisting of evenly-spaced, narrow modes ("comb teeth") underneath a broad spectral envelope (Cundiff and Ye, 2003; Hall, 2006; Hänsch, 2006). In DCS, two such frequency combs are used to measure the atmospheric absorption on a comb-tooth-by-tooth basis across broad bandwidths

[1] In this work we use dry mole fraction. ppm is defined as micromoles of CO_2 per mole of dry air and ppb is defined as nanomoles of CH_4 per mole of dry air.

Atmos. Meas. Tech. Discuss., doi:10.5194/amt-2017-62, 2017
Manuscript under review for journal Atmos. Meas. Tech.
Discussion started: 14 March 2017

Atmospheric Measurement Techniques Discussions

(Coddington et al., 2016; Ideguchi, 2017). As shown in Figure 1, two combs with nominal repetition rates of f_r and offset by Δf_r are phase locked together, transmitted through a sample, and their heterodyne signal measured on a photodetector. The resulting rf frequency comb can be mapped back to the optical domain to generate an overall spectrum, as shown in Figure 1(b), that is the product of the comb spectra and any atmospheric absorption. One important difference between DCS and other broad-band laser techniques is that here all wavelengths are measured at once rather than sequentially as would be the case for a swept laser system; as a result, DCS is much more immune to spectral distortions from turbulence effects. Moreover, for a fully phase-locked comb, as is used here, the optical frequency axis is stable and known to high accuracy, and the instrument lineshape is effectively the sum of two delta-functions, as shown in the spectrum in Figure 1(b). Alternatively, DCS can be thought of as high-resolution Fourier-transform spectroscopy with diffraction-limited light sources, no moving parts, negligible instrument line shape, and a rapid scanning rate of $1/\Delta f_r$, which we tune to be faster than turbulence-induced intensity variations. Here, both combs are transmitted over the open path yielding the atmospheric absorption spectrum, but it is also possible to transmit only a single comb through the air to measure both dispersion and absorbance (Giorgetta et al., 2015; Coddington et al., 2016).

Figure 2 provides an overview of our experiment. Two DCS instruments measured the atmospheric absorption across a 2-km-roundtrip open path that extended from the top of a building at the National Institute of Standards and Technology (NIST) Boulder campus to a pair of retroreflectors located on a nearby hill. Both DCS instruments were based on a similar overall design and used self-referenced, stabilized frequency combs (Sinclair et al., 2015), but one was built by a team at NIST and the other by a team at the University of Colorado; they are hereafter referred to as DCS A and DCS B, respectively. As outlined below, the two instruments differed in their exact design and physical parameters. Nevertheless, no instrument-specific calibration or bias offset was applied to either system. The acquired atmospheric absorption spectra were fit to retrieve the column density of CO_2, CH_4, and H_2O (as well as HDO and $^{13}CO_2$ at lower precision) along with the path-averaged temperature from the CO_2 spectrum. From these data, combined with the measured atmospheric pressure and the path length (measured via time-of-flight laser ranging), we retrieved the path-averaged dry mole fractions as a function of time, which are compared between DCS instruments and to a nearby cavity ringdown (CRDS) point sensor.

2.2 Dual comb spectrometer

Figure 3(a) shows a simplified schematic of both DCS setups. Briefly, each DCS system used two mutually coherent self-referenced erbium-doped fiber frequency combs based on the design of (Sinclair et al., 2015) with nominal repetitions rates and Δf_r given in Table 1. Mutual optical coherence between the combs is enforced by phase-locking an optical tooth of each to a common cw laser and the carrier-envelope offset frequency of each to a common quartz microwave oscillator. Absolute frequency accuracy is then enforced by a bootstrapped approach that effectively locks the common cw laser to the same quartz microwave oscillator (Truong et al., 2016). The result is sub-Hz mutual coherence, ~120-kHz absolute linewidths, and 3.6 x 10^{-5} cm^{-1} absolute frequency accuracy (Truong et al., 2016). This linewidth is orders of magnitude lower than the ~5 GHz or ~0.2 cm^{-1} width of pressure-broadened absorption lines. The direct output of the combs is spectrally broadened in highly nonlinear fiber to cover 7140-5710 cm^{-1} (1.4-1.75 µm) and then filtered to isolate the spectral region of interest from 6021 to 6388 cm^{-1} (1565 to 1661 nm).

The combined light from both combs is transmitted via single-mode fiber to a telescope, where it is launched to a retroreflector. The returning signal is collected onto an amplified, 100-MHz-bandwidth InGaAs photodetector and digitized at f_r. We acquire a single interferogram at a period of $1/\Delta f_r$ or 1.6 ms for DCS A; 100 such interferograms are directly summed in real time on a field-programmable gate array (FPGA). These are transferred to a computer where they are carrier-phase

Atmos. Meas. Tech. Discuss., doi:10.5194/amt-2017-62, 2017
Manuscript under review for journal Atmos. Meas. Tech.
Discussion started: 14 March 2017

Atmospheric Measurement Techniques Discussions

corrected and further summed over an acquisition time of ~30 seconds. These summed interferograms are then Fourier transformed and scaled, using the known optical frequency comb tooth positions, to generate a transmission spectrum (e.g. Figure 4a) spanning 367 cm^{-1} (>10 THz) with a point spacing of 0.0067 cm^{-1}.

The exact optical layout of DCS A is given in (Truong et al., 2016). While following the same basic design, DCS B differs in several technical details. These include a slightly different output spectrum, as well as slight different comb tooth spacings and offset frequency, minor differences in the reference cw laser and its locking scheme, and different amplifier design, launched and received powers, and telescope design. Some of these differences are laid out in Figure 3, Table 1, and Section 2.3 below.

We have found that the use of stabilized, phase coherent frequency combs is a necessary but not sufficient prerequisite to reaching sub-percent agreement in retrieved gas concentrations. It is critical that the spectrally-filtered comb output does not include stray unfiltered light. Similarly, any stray reflections from the telescope that can "short circuit" the atmospheric path must be avoided. As with FTIR systems, nonlinearities are problematic. In the optical domain, nonlinearities can arise when the combs are combined in fiber with high optical power. These are minimized for DCS A by filtering the light, which decreases the peak powers, before combining the combs. For DCS B the combs do not have a booster amplifier and thus have significantly lower power. Nonlinearities in the photodetection can also occur (Zolot et al., 2013); in laboratory tests with a CO reference cell, we verified no bias in retrieved concentration as a function of received power up to 300 μW, which is a factor of two higher than the maximum power for the open path data. It was also critical to match the interferogram amplitude to the full dynamic range of the analog-to-digital converters (ADCs) to avoid effective nonlinearities in the digitization process.

2.3 Launch/Receive telescope

The two telescope systems are shown in Figure 3(a). Due to the large spectral bandwidth, reflective optics are preferred to minimize chromatic dispersion. For DCS A, the launch/receive system was based on a bi-directional off-axis parabolic telescope with a 3" aperture while for DCS B, it was based on a 6"-aperture Ritchey-Chretien (RC) telescope with the light launched separately from behind the secondary mirror. In both cases, the launched beam diameter was ~ 40 mm and the light was directed to a hollow corner-cube retroreflector of 2.5" (DCS A) or 5" (DCS B) diameter. A slow servo was implemented for long-term pointing of the telescope to the retroreflectors. For this servo, a low-divergence 850 nm LED is co-aligned with the telescope and its retro-reflected light is detected by a co-aligned CMOS camera with a long focal-length lens and an 850-nm-bandpass optical filter. We then servo the overall telescope pointing via its gimbal using the LED spot location on the camera. Further servo details are described in Cossel et al. (2017).

Figure 3(b) shows the return power for both systems as a function of time. For reference, the minimum return power required to obtain useful spectra was ~15 μW (horizontal black line). At lower powers, the acquired individual spectra are excluded. Turbulence-induced intensity variations are lower for the RC-telescope than the off-axis parabolic telescope because of its larger aperture; however, the long-term stability of the off-axis parabolic telescope was better due to a higher-quality gimbal system. The collection efficiency of the 6" RC telescope system was about 10-20% in low to moderate turbulence (C_n^2 of 10^{-14}). The collection efficiency of the off-axis parabolic telescope system was lower, at ~ 2-4% in similar conditions, due to 1) the smaller collection aperture and 2) the 50:50 beam splitter, which causes a factor of 4 loss. Attempts to replace the 50:50 splitter with a polarizing beam splitter and quarter-wave plate combination increased the collection efficiency but introduced additional etalons across the spectrum and for this reason was not used.

2.4 Data processing

Atmos. Meas. Tech. Discuss., doi:10.5194/amt-2017-62, 2017
Manuscript under review for journal Atmos. Meas. Tech.
Discussion started: 14 March 2017

Atmospheric Measurement Techniques Discussions

The acquired transmission spectra are the product $S(v) = I_0(v) \times e^{-A(v)}$, where I_0 is the geometric mean of the two individual comb spectra, $A(v)$ is the desired atmospheric absorbance, and v is the average optical frequency of the two participating comb teeth, (e.g. Fig. 1(b)). We fit the natural logarithm of the transmission spectra, $-\ln[S(v)] = -\ln[I_0(v)] + A(v)$, where the first term is represented by a piecewise polynomial and the second by an absorption spectrum calculated from a spectral database with floated concentrations of $^{12}CO_2$, $^{13}CO_2$, $^{12}CH_4$, $^{13}CH_4$, H_2O, and HDO. For a spectral database we use HITRAN 2008 (Rothman et al., 2009) and Voigt lineshapes as this generates a consistent set of line parameters across our conditions and gases. The fit is performed in three steps: first, we fit the polynomial (typically 7th order) over small windows (typically 100 GHz or 3.33 cm^{-1}) and include the expected absorbance from relevant gas absorption lines. These polynomials are then stitched together to generate the overall polynomial baseline, which is removed from the measured spectrum to find $A(v)$. We then fit only the 30013 ← 00001 CO_2 band in order to retrieve the path-averaged temperature. Finally, $A(v)$ is then re-fit over the entire spectral window by floating the gas concentrations at the retrieved path-averaged temperature. The retrieved path-averaged concentrations are converted to wet mole fractions by normalizing to the total number density of air molecules, which is calculated from the fitted (or separately measured) air temperature combined with the atmospheric pressure, as measured by a sensor co-located with the CRDS sensor and corrected for the altitude difference. Finally, wet CO_2, $^{13}CO_2$, and CH_4 are converted to dry values (XCO_2, $X^{13}CO_2$, XCH_4) using $XS = S/(1-c_{H2O})$ where XS is the dry species concentration, S is the retrieved wet species concentration and c_{H2O} is the retrieved H_2O volume mole fraction.

3 Intercomparison Results and Discussion

3.1 Atmospheric spectrum comparison

Figure 4(a) shows the overall raw DCS transmission spectra from the two instruments averaged for a three-hour period. They differ significantly because of the different comb intensity profiles, $I_0(v)$. However, after the polynomial baseline fit discussed above is applied, the resulting 3-hour averaged absorption spectra are nearly identical as shown in Figure 4(b). The inset of Figure 4(b) shows the data sampling points (spaced at ~200 MHz) across several absorption lines with width of 5 GHz 0.2 cm^{-1}) indicating we have sufficient optical resolution to over-sample the lines. The difference of the absorption spectra, shown as the black line in Figure 4(c), has a standard deviation of 9×10^{-4} with no observable structure at absorption lines. This difference is dominated by an etalon on the off-axis telescope used with DCS A. After manually fitting out the etalon structure, DCS A and DCS B agree to better than 5×10^{-4} (limited by the instrumental noise level) over the full spectral region (with the exception of a 7 cm^{-1} section at 6290 cm^{-1}), and better than 2.5×10^{-4} over the region near 6100 cm^{-1} where both DCS systems have significant returned optical power. This very high level of agreement between the two spectra shows that there are no instrumental line shapes or detector nonlinearity effects distorting the observed spectral line shapes; otherwise, structure would be observed in the difference. Thus, the two DCS instruments measure the same comb-tooth-resolved atmospheric absorbance spectrum.

Figure 4(d) shows the residuals after fitting the absorption lines in the DCS A spectrum to HITRAN 2008 and removing the etalon. The higher SNR of the DCS A yields an even lower broadband noise than the difference spectrum, but there are clear residuals near spectral lines attributable to incorrect line shapes/parameters in the HITRAN 2008 database. Nevertheless, the overall magnitude of the residuals is very small in comparison to the spectral absorption.

3.2 Comparison of retrieved mole fractions from DCS A and DCS B

From the fitted concentrations, we retrieve the mole fractions as outlined in Section 2.4. The retrieved time series for XCO_2, $X^{13}CO_2$, XCH_4, H_2O, and HDO are given in Figure 5 at ~30 second intervals.

Atmos. Meas. Tech. Discuss., doi:10.5194/amt-2017-62, 2017
Manuscript under review for journal Atmos. Meas. Tech.
Discussion started: 14 March 2017

Atmospheric Measurement Techniques Discussions

Gaps in the data are due to either telescope misalignment (primarily on the 6" RC telescope due to the lower-quality gimbal system) or, more rarely, a loss of phase lock of one of the four frequency combs. Excellent agreement is observed between both systems for all retrieved concentrations. Figure 6 shows the concentration differences, which exhibit a high-frequency white noise consistent with the quadrature sum of the DCS precisions given in Section 3.3. In addition, the differences show a slow wander about zero indicating slowly changing, small offsets between the two DCS instruments. CH_4 also shows a small negative offset for the second week of the campaign. A Gaussian curve approximates the distribution of the differences over the full two weeks reasonably well and is shown in Figure 7. At 32-second averaging times, the mean and width of the distributions are $\Delta XCO_2 = 0.57 \pm 2.4$ ppm, $\Delta XCH_4 = -7.0 \pm 16$ ppb, $\Delta c_{H2O} = 36 \pm 90$ ppm, and $\Delta c_{HDO} = 390 \pm 860$ ppm. These widths decrease to 1.5 ppm, 12 ppb, 66 ppm, and 480 ppm, respectively, for 5-minute averaging times. These mean values correspond to a relative offset of 0.14 % CO_2, -0.35 % CH_4, and 0.4 % H_2O and are close to the WMO compatibility standards of 0.1 ppm for CO_2 and 2 ppb for CH_4 (Tans and Zellweger, 2015). We emphasize the agreement here is achieved over a two-week period despite outdoor temperature variations of 4.6 to 28.9 °C, DCS instrument ambient temperature variations from 17 to 25 °C, 10% to 90% relative humidity fluctuations, and large turbulence-induced return power fluctuations.

Table 2 summarizes the systematic uncertainties of the DCS systems. The choice of spectral model effectively sets the calibration that converts the measured absorbance spectrum to path-averaged concentrations. The temperature primarily affects the conversion of the path-averaged concentration to mole fractions (through the calculation of the overall air concentration). For the direct intercomparison, both DCS data were analyzed with a common spectral model (HITRAN 2008) and temperature in order to separate out instrument-specific systematics from the more fundamental connection between absorption and concentration. Below we discuss these instrument-specific systematics (given in the top part of Table 2). A discussion of the uncertainties from the spectral model and temperature (given in the bottom part of Table 2) is given in Section 3.5.

To explore the source of the small systematic offsets between the DCS retrievals, we have performed a number of control comparisons. In the processing, we have varied the initial concentration guess in the fit with negligible effect. We have also varied the polynomial baseline fit by adjusting the window size from 100 to 150 GHz and polynomial order from 7th to 9th order and again found negligible variations of 0.02 % for CO_2 (<0.07 ppm), 0.07% for CH_4 (<1.4 ppb), and 0.05% (~4 ppm) for H_2O. In laboratory tests, we verified that the two DCS instruments retrieve the same CO_2 concentrations to within 0.04% for 8450 ppm of CO_2 in a 30-meter multipass cell (roughly mimicking the total absorption over the open path). In open-path tests, we have separated effects of the detection/acquisition system and optical system. First, the detected DCS A return signal was split to the two separate data acquisition systems. The two processed signals yielded small differences of 0.16 ppm CO_2, 0.34 ppb CH_4, and 1.0 ppm H_2O, presumably due to residual nonlinearities and reflections in the rf system and digitization. Second, the outgoing DCS A comb light was split and directed to the two different telescopes and acquisition systems. These two processed signals yielded larger differences of 0.45 ppm CO_2, 1.5 ppb CH_4, and 56 ppm H_2O, possibly due to scattered light or polarization dependences in the launch and receive optical systems. Finally, residual phase noise between the two combs in a single DCS system can cause small biases in the retrieved concentrations, but these should be well below 0.1% in this configuration (Truong et al. 2017, in prep). All these instrument uncertainties are summarized in Table 2.

3.3 DCS precision

Figure 8 shows the precision versus averaging time (determined using the modified Allan deviation) based on the scatter across a 6-hour period over which the CO_2 and CH_4 concentrations are reasonably flat, shown as the highlighted part of Figure 5. (The Allan deviation for H_2O is not calculated because the atmospheric H_2O concentration varies significantly over this time period.) Under perfectly

Atmos. Meas. Tech. Discuss., doi:10.5194/amt-2017-62, 2017
Manuscript under review for journal Atmos. Meas. Tech.
Discussion started: 14 March 2017

Atmospheric Measurement Techniques Discussions

stable concentrations and white instrument noise, the precision should decrease as the square root of averaging time, indicated as a grey line in Figure 8. Initially, the Allan deviations do follow this slope, but the atmospheric concentrations, especially of CO_2, vary over this 6-hour period and the Allan deviations reach a floor at ~ 1000 s.

The precision at 30-second and 5-minute averaging time is given at the bottom of Table 1. DCS A has superior CO_2 precision because it has higher received optical comb power in that spectral region, whereas the DCS instruments have similar received power in the CH_4 spectral region and therefore similar CH_4 precisions. Regardless, the precision of either instrument is sufficiently high to measure the characteristic atmospheric fluctuations of these gases on tens-of-seconds timescales.

3.4 Comparison of open-path DCS to a cavity ringdown point sensor (CRDS)

A commercial cavity-ringdown point sensor, Picarro Model 1301[2] (Crosson, 2008), was also located along the path as shown in Figure 2. Its inlet was 30 m above ground on a radio tower, approximately 160 m perpendicular to the DCS beam path. Figure 9 compares the DCS A and CRDS (smoothed to 32-s resolution) time series. In general, their overall shapes agree well with both systems tracking ~40 ppm variations in XCO_2, 200 ppb variations in XCH_4, and 1% variations in H_2O over days. Nevertheless, there are clear discrepancies in terms of both short-duration spikes and a long-term overall offset between the DCS and CRDS time series.

The short-duration spikes are present in the CRDS time series and presumably arise from the very different spatial sampling of the two instruments. The DCS system measures the integrated column over one kilometer (one way), while the CRDS is a point sensor and therefore much more sensitive to local sources. For example, a 1 m^3 volume of air containing 500 ppm of CO_2 from a vehicle driving under the sampling line will result in a sharp spike in the CRDS data as the air mass passes the sampling inlet. However, that same air mass will result in only a 0.025% or 0.1 ppm increase in the DCS path-averaged concentration (assuming a 400 ppm background). These spikes in the CRDS time series are damped here by the 32-second smoothing but are occasionally evident especially during the second week. The general scarcity of such events does suggest that the air over the open path is usually fairly well mixed.

The long-term overall offset between the CRDS and DCS data is a consequence of their very different calibrations. The CRDS is tied to the WMO scale for CO_2 and CH_4 by directly injecting known dry WMO-calibrated CO_2/CH_4 mixtures at different trace gas concentrations and different water vapor concentrations into its temperature- and pressure-controlled sampling cavity. This instrument was calibrated shortly after the measurement campaign and should thus have an absolute uncertainty close to that of the WMO-scale uncertainties of ~ 0.07 ppm for CO_2 (Zhao and Tans, 2006) and ~1.5 ppb for CH_4 (Dlugokencky et al., 2005). In contrast, the DCS has no instrument-specific calibration but relies completely on a fit to a spectral database to extract the gas concentrations from the measured absorbance across a wide range of ambient pressures and temperatures. Here, we use HITRAN 2008 which has $^{12}CO_2$ linestrength uncertainties of 1-2 %, $^{12}CH_4$ linestrength uncertainties of 10-20%, and $H_2{}^{16}O$ linestrength uncertainties of 5-10% (Rothman et al., 2009), leading to a poorer absolute calibration than the WMO-calibrated point sensor. From the data in Figure 9, the differences between the CRDS and DCS data across the two-week period are -3.4 ± 3.4 ppm CO_2, 17 ± 15 ppb CH_4, and 580 ± 462 ppm H_2O at 5-minute averaging. These correspond to relative offsets of -0.85% for CO_2, 0.94% for CH_4, and 6.9% for H_2O, well within the stated uncertainties of HITRAN 2008. In previous DCS measurements, we found slightly different offsets, specifically 1.78% for CO_2, 0.20% for CH_4, and 1.74% for H_2O in (Rieker et al., 2014) and ~1 % for CO_2 in (Giorgetta et al., 2015). However, these previous data

[2] The use of trade names is necessary to specify the experimental results and does not imply endorsement by the National Institute of Standards and Technology.

covered much shorter timespans, used an older CRDS point sensor calibration, and may have included small systematic offsets in the DCS systems due to technical issues discussed in Section 3.2.

This basic discrepancy between retrievals based on lineshape parameters from a spectral database and manometric calibrations (WMO standard) is not unique to DCS. Several studies have calibrated the Total Carbon Column Observing Network (TCCON) retrievals against WMO-based instruments (Wunch et al., 2010; Messerschmidt et al., 2011; Geibel et al., 2012; Tanaka et al., 2012). Although TCCON is not a solely HITRAN-based analysis (Wunch et al., 2011), a correction factor of 0.9898 for CO_2, 0.9765 for CH_4, and 1.0183 for H_2O (Wunch et al., 2010) is needed to bring the overall TCCON retrievals into agreement with the WMO-based data. Additionally, theoretical calculations by (Zak et al., 2016) found an approximately 0.5% difference between CO_2 line parameters from HITRAN 2012 and their density functional theory calculations and an additional 0.5% difference between the calculations and new measurements by (Devi et al., 2016) in the 1.6-micron region. Certainly this discrepancy between retrievals from HITRAN and WMO-calibrated instruments is not fundamental and further experimental work should lead to improved spectral database parameters and much better agreement. As noted in earlier work on CO_2, it will be important to establish both the correct linestrengths as well as account for complex lineshapes and line mixing (e.g. Devi et al., 2007; Thompson et al., 2012; Bui et al., 2014; Long et al., 2015; Devi et al., 2016). A direct comparison of the open-path DCS spectra acquired here and laboratory DCS spectra acquired for WMO-calibrated gas samples can contribute to these future improvements and is planned. Finally, we emphasize that because the DCS instruments record the atmospheric absorption without instrument distortions, as spectral models improve, past open-path spectra can be refit with reduced uncertainty.

An accurate path-averaged air temperature is also important to avoid systematic offsets. Unlike vertical total-column measurements through the entire atmosphere, km-scale open horizontal paths should have relatively low temperature inhomogeneities of around a few degrees C, and thus the use of a single “path averaged” temperature in the fit is sufficient for accurate retrievals. We verified this through a sensitivity study comparing retrievals for simulated spectra with temperature gradients up to 10 °C over the path; the resulting bias was below 0.03 ppm CO_2 (0.007%) and 0.4 ppb CH_4 (0.022%), as shown in Table 2. On the other hand, any error in the path-averaged temperature can bias the mole fractions through two effects. First, the retrieved path-averaged concentration will vary weakly with temperature because of temperature-dependent line parameters. Second and dominantly, the final mole fraction calculation requires normalization by the air density. Here, this density is calculated from the ideal gas law using the measured air pressure and path-averaged temperature. Therefore, a fractional error in temperature leads to a corresponding fractional error in mole fraction. For example, a 0.15% uncertainty in mole fraction requires 0.5 °C uncertainty in the path-averaged air temperature. (See Table 2.) We verified that this simple linear relationship is valid up to a temperature uncertainty of 10 °C in a sensitivity study. From the discussion in Appendix A, the use of a point temperature sensor near the end of the open path is clearly insufficient to achieve <0.5 °C uncertainty at many times of the day. Instead, for the data here, we have used the fitted path-averaged temperature, as discussed in Section 2.4. The approach effectively relies on the spectral database but, in this case, on the variation in the Boltzmann distribution of the J-level population with temperature. In Table 2, we have taken a hopefully conservative uncertainty of 0.5 °C for the path-averaged temperature, but more work is needed to establish the true uncertainty from these retrieved values. Finally, we note the fractional uncertainty in the measured atmospheric pressure from the sensor or altitude-based pressure changes across the optical path was below 0.36%.

4. Diurnal cycles and source analysis

The two weeks of open path data are analyzed for diurnal cycles, as shown in Figure 10 with the intent of an initial understanding of CO_2 and CH_4 sources. For this analysis, the wind speed and wind direction

were taken from the NCAR Mesa weather data (ftp://ftp.eol.ucar.edu/pub/archive/weather/mesa/), while the gas concentrations are from DCS A.

4.1 Carbon dioxide

As expected, the median of the diurnal cycle for CO_2 shows a peak in the early to mid-morning from commuter traffic after which the CO_2 concentration decreases as the boundary layer rises. It remains approximately steady throughout the afternoon, decreases to a minimum between 19:00 and 20:00, and then increases slightly overnight as the boundary layer collapses. We hypothesize that the afternoon behavior is due to the change in wind direction. Often overnight and through early morning the wind blows from the west to southwest, which brings in cleaner background air from the mountains bordering Boulder. However, in late morning the predominant wind direction shifts to the east and southeast, possibly bringing in higher CO_2 concentrations from the Denver metropolitan area – which lies approximately 30 km to the southeast of Boulder – over the course of the afternoon. Typically, the evening wind shifts back to out of the west, once again bringing in the cleaner mountain air and with it a decrease in CO_2 concentration.

4.2 Methane

Methane has a significantly weaker diurnal cycle than carbon dioxide, which is consistent with a species that lacks significant diurnally-varying local sources. Rather, its concentration follows expected variations in the boundary layer height; the concentration increases overnight into the early morning as the boundary layer collapses, and then decreases during the late morning through afternoon as the boundary layer rises again. The largest likely methane source near Boulder is local oil/gas fields, but these typically lie to the northeast, while the wind directions are generally out of the west to southeast. It is also possible that the methane comes from leaking natural gas infrastructure within the city.

5 Conclusions

Here we provide the first quantitative comparison of open-path dual comb spectroscopy instruments. The dual-comb spectrometers were based on fully phase-coherent and stabilized fiber frequency combs and operated nearly continuously over a two-week period. We performed these measurements over adjacent 2-kilometer round-trip paths to measure concentrations of dry CO_2, dry CH_4, H_2O, and HDO. The measured atmospheric absorbance spectra agree to better than 10^{-3}. Correspondingly, we find excellent agreement between the retrieved concentrations from the two instruments without the need for instrument calibration: over two weeks of near-continuous measurements, the retrieved CO_2 concentrations agree to better than 0.14% (0.57 ppm), CH_4 concentrations agrees to better than 0.35% (7.0 ppb), and H_2O concentrations agrees to better than 0.4% (36 ppm). These values are very close to the WMO compatibility goals. The remaining disagreement is likely due to scattered stray light, polarization dependencies, and residual comb phase noise. We further compare the DCS measurements to a cavity ringdown point sensor located along our path. The measured dry CO_2 mole fraction agrees to within 1%, the CH_4 dry mole fraction to within 1.2%, and H_2O mole fraction to within 6.2%. However, this CRDS point sensor is directly calibrated to the WMO scale for CO_2 and CH_4 while the DCS results are based on HITRAN 2008; we attribute the disagreement in CO_2 and CH_4 to inaccurate line parameters in the HITRAN database. (Most of the water discrepancy is attributed to the imperfect absolute water calibration of the CRDS point sensor.) Further improvements to the spectral database should reduce these discrepancies. Finally, this open-path DCS can exploit even broader spectrum combs up to 2.3 µm and down to 1.1 µm (Zolot et al., 2012; Okubo et al., 2015), which would enable measurements of similar quality for $^{13}CO_2$, NH_3, N_2O, and O_2. These results make open-path DCS a promising new system for greenhouse gas flux measurements from distributed sources.

The authors declare that they have no conflict of interest.

Acknowledgements: We thank T. Newburger and K. McKain for assistance with the CRDS calibrations, T. Bullet and J. Kofler for assistance in setting up the CRDS sampling, and R. Thalman for detailed long-path instrument correlation data, and A.J. Fleischer and A. Karion for assistance with the manuscript. This work was funded by the Defense Advanced Research Program Agency DSO SCOUT program, ARPA-E MONITOR program under Award Number DE-AR0000539, and the NIST Greenhouse Gas and Climate Science Initiative. EMW and KCC are supported by National Research Council postdoctoral fellowships.

References

Bui, T. Q., Long, D. A., Cygan, A., Sironneau, V. T., Hogan, D. W., Rupasinghe, P. M., Ciuryło, R., Lisak, D. and Okumura, M.: Observations of Dicke narrowing and speed dependence in air-broadened CO_2 lineshapes near 2.06 µm, J. Chem. Phys., 141(17), 174301, doi:10.1063/1.4900502, 2014.

Ciais, P., Rayner, P., Chevallier, F., Bousquet, P., Logan, M., Peylin, P. and Ramonet, M.: Atmospheric inversions for estimating CO_2 fluxes: methods and perspectives, Clim. Change, 103(1–2), 69–92, doi:10.1007/s10584-010-9909-3, 2010.

Coddington, I., Swann, W. C. and Newbury, N. R.: Coherent multiheterodyne spectroscopy using stabilized optical frequency combs, Phys. Rev. Lett., 100(1), 013902, doi:10.1103/PhysRevLett.100.013902, 2008.

Coddington, I., Newbury, N. and Swann, W.: Dual-comb spectroscopy, Optica, 3(4), 414, doi:10.1364/OPTICA.3.000414, 2016.

Conde, V., Robidoux, P., Avard, G., Galle, B., Aiuppa, A., Muñoz, A. and Giudice, G.: Measurements of volcanic SO_2 and CO_2 fluxes by combined DOAS, Multi-GAS and FTIR observations: a case study from Turrialba and Telica volcanoes, Int. J. Earth Sci., 103(8), 2335–2347, doi:10.1007/s00531-014-1040-7, 2014.

Crosson, E. R.: A cavity ring-down analyzer for measuring atmospheric levels of methane, carbon dioxide, and water vapor, Appl. Phys. B, 92(3), 403–408, doi:10.1007/s00340-008-3135-y, 2008.

Devi, V. M., Benner, D. C., Brown, L. R., Miller, C. E. and Toth, R. A.: Line mixing and speed dependence in CO_2 at 6227.9 cm^{-1}: Constrained multispectrum analysis of intensities and line shapes in the 30013 ← 00001 band, J. Mol. Spectrosc., 245(1), 52–80, doi:10.1016/j.jms.2007.05.015, 2007.

Devi, V. M., Benner, D. C., Sung, K., Brown, L. R., Crawford, T. J., Miller, C. E., Drouin, B. J., Payne, V. H., Yu, S., Smith, M. A. H., Mantz, A. W. and Gamache, R. R.: Line parameters including temperature dependences of self- and air-broadened line shapes of 12C16O2: 1.6-µm region, J. Quant. Spectrosc. Radiat. Transf., 177, 117–144, doi:10.1016/j.jqsrt.2015.12.020, 2016.

Dlugokencky, E. J., Myers, R. C., Lang, P. M., Masarie, K. A., Crotwell, A. M., Thoning, K. W., Hall, B. D., Elkins, J. W. and Steele, L. P.: Conversion of NOAA atmospheric dry air CH_4 mole fractions to a gravimetrically prepared standard scale, J. Geophys. Res. Atmospheres, 110(D18), D18306, doi:10.1029/2005JD006035, 2005.

466 EPA: EPA Handbook: Optical Remote Sensing for Measurement and Monitoring of Emissions, [online]
467 Available from: https://www3.epa.gov/ttn/emc/guidlnd/gd-052.pdf (Accessed 2 March 2017), n.d.

468 Frey, M., Hase, F., Blumenstock, T., Groß, J., Kiel, M., Mengistu Tsidu, G., Schäfer, K., Sha, M. K. and
469 Orphal, J.: Calibration and instrumental line shape characterization of a set of portable FTIR
470 spectrometers for detecting greenhouse gas emissions, Atmos Meas Tech, 8(7), 3047–3057,
471 doi:10.5194/amt-8-3047-2015, 2015.

472 Geibel, M. C., Messerschmidt, J., Gerbig, C., Blumenstock, T., Chen, H., Hase, F., Kolle, O., Lavrič, J. V.,
473 Notholt, J., Palm, M., Rettinger, M., Schmidt, M., Sussmann, R., Warneke, T. and Feist, D. G.: Calibration
474 of column-averaged CH_4 over European TCCON FTS sites with airborne in-situ measurements, Atmos
475 Chem Phys, 12(18), 8763–8775, doi:10.5194/acp-12-8763-2012, 2012.

476 Giorgetta, F. R., Rieker, G. B., Baumann, E., Swann, W. C., Sinclair, L. C., Kofler, J., Coddington, I. and
477 Newbury, N. R.: Broadband Phase Spectroscopy over Turbulent Air Paths, Phys. Rev. Lett., 115(10),
478 103901, doi:10.1103/PhysRevLett.115.103901, 2015.

479 Hak, C., Pundt, I., Trick, S., Kern, C., Platt, U., Dommen, J., Ordóñez, C., Prévôt, A. S. H., Junkermann, W.,
480 Astorga-Lloréns, C. and others: Intercomparison of four different in-situ techniques for ambient
481 formaldehyde measurements in urban air, Atmospheric Chem. Phys., 5(11), 2881–2900, 2005.

482 Hedelius, J. K., Viatte, C., Wunch, D., Roehl, C. M., Toon, G. C., Chen, J., Jones, T., Wofsy, S. C., Franklin, J.
483 E., Parker, H., Dubey, M. K. and Wennberg, P. O.: Assessment of errors and biases in retrievals of XCO_2,
484 XCH_4, XCO, and XN_2O from a 0.5 cm^{-1} resolution solar-viewing spectrometer, Atmos Meas Tech, 9(8),
485 3527–3546, doi:10.5194/amt-9-3527-2016, 2016.

486 Lauvaux, T. and Davis, K. J.: Planetary boundary layer errors in mesoscale inversions of column-
487 integrated CO_2 measurements, J. Geophys. Res. Atmospheres, 119(2), 490–508,
488 doi:10.1002/2013JD020175, 2014.

489 Lauvaux, T., Uliasz, M., Sarrat, C., Chevallier, F., Bousquet, P., Lac, C., Davis, K. J., Ciais, P., Denning, A. S.
490 and Rayner, P. J.: Mesoscale inversion: first results from the CERES campaign with synthetic data, Atmos
491 Chem Phys, 8(13), 3459–3471, doi:10.5194/acp-8-3459-2008, 2008.

492 Lauvaux, T., Schuh, A. E., Bocquet, M., Wu, L., Richardson, S., Miles, N. and Davis, K. J.: Network design
493 for mesoscale inversions of CO_2 sources and sinks, Tellus B, 64(0), doi:10.3402/tellusb.v64i0.17980,
494 2012.

495 Long, D. A., Wójtewicz, S., Miller, C. E. and Hodges, J. T.: Frequency-agile, rapid scanning cavity ring-
496 down spectroscopy (FARS-CRDS) measurements of the (30012)←(00001) near-infrared carbon dioxide
497 band, J. Quant. Spectrosc. Radiat. Transf., 161, 35–40, doi:10.1016/j.jqsrt.2015.03.031, 2015.

498 Messerschmidt, J., Geibel, M. C., Blumenstock, T., Chen, H., Deutscher, N. M., Engel, A., Feist, D. G.,
499 Gerbig, C., Gisi, M., Hase, F., Katrynski, K., Kolle, O., Lavrič, J. V., Notholt, J., Palm, M., Ramonet, M.,
500 Rettinger, M., Schmidt, M., Sussmann, R., Toon, G. C., Truong, F., Warneke, T., Wennberg, P. O., Wunch,
501 D. and Xueref-Remy, I.: Calibration of TCCON column-averaged CO_2: the first aircraft campaign over
502 European TCCON sites, Atmos Chem Phys, 11(21), 10765–10777, doi:10.5194/acp-11-10765-2011, 2011.

503 Okubo, S., Iwakuni, K., Inaba, H., Hosaka, K., Onae, A., Sasada, H. and Hong, F.-L.: Ultra-broadband dual-
504 comb spectroscopy across 1.0–1.9 μm, Appl. Phys. Express, 8(8), 082402, doi:10.7567/APEX.8.082402,
505 2015.

506 Reiche, N., Westerkamp, T., Lau, S., Borsdorf, H., Dietrich, P. and Schütze, C.: Comparative study to
507 evaluate three ground-based optical remote sensing techniques under field conditions by a gas tracer
508 experiment, Environ. Earth Sci., 72(5), 1435–1441, doi:10.1007/s12665-014-3312-8, 2014.

509 Rieker, G. B., Giorgetta, F. R., Swann, W. C., Kofler, J., Zolot, A. M., Sinclair, L. C., Baumann, E., Cromer,
510 C., Petron, G., Sweeney, C., Tans, P. P., Coddington, I. and Newbury, N. R.: Frequency-comb-based
511 remote sensing of greenhouse gases over kilometer air paths, Optica, 1(5), 290–298,
512 doi:10.1364/OPTICA.1.000290, 2014.

513 Rothman, L. S., Gordon, I. E., Barbe, A., Benner, D. C., Bernath, P. E., Birk, M., Boudon, V., Brown, L. R.,
514 Campargue, A., Champion, J. P., Chance, K., Coudert, L. H., Dana, V., Devi, V. M., Fally, S., Flaud, J. M.,
515 Gamache, R. R., Goldman, A., Jacquemart, D., Kleiner, I., Lacome, N., Lafferty, W. J., Mandin, J. Y.,
516 Massie, S. T., Mikhailenko, S. N., Miller, C. E., Moazzen-Ahmadi, N., Naumenko, O. V., Nikitin, A. V.,
517 Orphal, J., Perevalov, V. I., Perrin, A., Predoi-Cross, A., Rinsland, C. P., Rotger, M., Simeckova, M., Smith,
518 M. A. H., Sung, K., Tashkun, S. A., Tennyson, J., Toth, R. A., Vandaele, A. C. and Vander Auwera, J.: The
519 HITRAN 2008 molecular spectroscopic database, J. Quant. Spectrosc. Radiat. Transf., 110(9–10), 533–
520 572, doi:10.1016/j.jqsrt.2009.02.013, 2009.

521 Shao, L., Wang, W., Griffiths, P. R. and Leytem, A. B.: Increasing the Quantitative Credibility of Open-Path
522 Fourier Transform Infrared (FT-IR) Spectroscopic Data, with Focus on Several Properties of the
523 Background Spectrum, Appl. Spectrosc., 67(3), 335–341, doi:10.1366/12-06901, 2013.

524 Sinclair, L. C., Deschênes, J.-D., Sonderhouse, L., Swann, W. C., Khader, I. H., Baumann, E., Newbury, N. R.
525 and Coddington, I.: Invited Article: A compact optically coherent fiber frequency comb, Rev. Sci.
526 Instrum., 86(8), 081301, doi:10.1063/1.4928163, 2015.

527 Smith, T. E. L., Wooster, M. J., Tattaris, M. and Griffith, D. W. T.: Absolute accuracy and sensitivity
528 analysis of OP-FTIR retrievals of CO_2, CH_4 and CO over concentrations representative of “clean air” and
529 “polluted plumes,” Atmos Meas Tech, 4(1), 97–116, doi:10.5194/amt-4-97-2011, 2011.

530 Tanaka, T., Miyamoto, Y., Morino, I., Machida, T., Nagahama, T., Sawa, Y., Matsueda, H., Wunch, D.,
531 Kawakami, S. and Uchino, O.: Aircraft measurements of carbon dioxide and methane for the calibration
532 of ground-based high-resolution Fourier Transform Spectrometers and a comparison to GOSAT data
533 measured over Tsukuba and Moshiri, Atmos Meas Tech, 5(8), 2003–2012, doi:10.5194/amt-5-2003-
534 2012, 2012.

535 Tans, P. and Zellweger, C.: 18th WMO/IAEA Meeting on Carbon Dioxide, Other Greenhouse Gases and
536 Related Tracers Measurement Techniques, GAW, La Jolla, CA, USA. [online] Available from:
537 http://www.wmo.int/pages/prog/arep/gaw/documents/FINAL_GAW_REPORT_229.pdf (Accessed 8
538 February 2017), 2015.

539 Thalman, R., Baeza-Romero, M. T., Ball, S. M., Borrás, E., Daniels, M. J. S., Goodall, I. C. A., Henry, S. B.,
540 Karl, T., Keutsch, F. N., Kim, S., Mak, J., Monks, P. S., Muñoz, A., Orlando, J., Peppe, S., Rickard, A. R.,
541 Ródenas, M., Sánchez, P., Seco, R., Su, L., Tyndall, G., Vázquez, M., Vera, T., Waxman, E. and Volkamer,

R.: Instrument intercomparison of glyoxal, methyl glyoxal and NO_2 under simulated atmospheric conditions, Atmos Meas Tech, 8(4), 1835–1862, doi:10.5194/amt-8-1835-2015, 2015.

Thoma, E. D., Shores, R. C., Thompson, E. L., Harris, D. B., Thorneloe, S. A., Varma, R. M., Hashmonay, R. A., Modrak, M. T., Natschke, D. F. and Gamble, H. A.: Open-Path Tunable Diode Laser Absorption Spectroscopy for Acquisition of Fugitive Emission Flux Data, J. Air Waste Manag. Assoc., 55(5), 658–668, doi:10.1080/10473289.2005.10464654, 2005.

Thompson, D. R., Chris Benner, D., Brown, L. R., Crisp, D., Malathy Devi, V., Jiang, Y., Natraj, V., Oyafuso, F., Sung, K., Wunch, D., Castaño, R. and Miller, C. E.: Atmospheric validation of high accuracy CO_2 absorption coefficients for the OCO-2 mission, J. Quant. Spectrosc. Radiat. Transf., 113(17), 2265–2276, doi:10.1016/j.jqsrt.2012.05.021, 2012.

Truong, G.-W., Waxman, E. M., Cossel, K. C., Baumann, E., Klose, A., Giorgetta, F. R., Swann, W. C., Newbury, N. R. and Coddington, I.: Accurate frequency referencing for fieldable dual-comb spectroscopy, Opt. Express, 24(26), 30495, doi:10.1364/OE.24.030495, 2016.

Wunch, D., Toon, G. C., Wennberg, P. O., Wofsy, S. C., Stephens, B. B., Fischer, M. L., Uchino, O., Abshire, J. B., Bernath, P., Biraud, S. C., Blavier, J.-F. L., Boone, C., Bowman, K. P., Browell, E. V., Campos, T., Connor, B. J., Daube, B. C., Deutscher, N. M., Diao, M., Elkins, J. W., Gerbig, C., Gottlieb, E., Griffith, D. W. T., Hurst, D. F., Jiménez, R., Keppel-Aleks, G., Kort, E. A., Macatangay, R., Machida, T., Matsueda, H., Moore, F., Morino, I., Park, S., Robinson, J., Roehl, C. M., Sawa, Y., Sherlock, V., Sweeney, C., Tanaka, T. and Zondlo, M. A.: Calibration of the Total Carbon Column Observing Network using aircraft profile data, Atmos Meas Tech, 3(5), 1351–1362, doi:10.5194/amt-3-1351-2010, 2010.

Wunch, D., Toon, G. C., Blavier, J.-F. L., Washenfelder, R. A., Notholt, J., Connor, B. J., Griffith, D. W. T., Sherlock, V. and Wennberg, P. O.: The Total Carbon Column Observing Network, Philos. Trans. R. Soc. Math. Phys. Eng. Sci., 369(1943), 2087–2112, doi:10.1098/rsta.2010.0240, 2011.

Zak, E., Tennyson, J., Polyansky, O. L., Lodi, L., Zobov, N. F., Tashkun, S. A. and Perevalov, V. I.: A room temperature CO_2 line list with ab initio computed intensities, J. Quant. Spectrosc. Radiat. Transf., 177, 31–42, doi:10.1016/j.jqsrt.2015.12.022, 2016.

Zhao, C. L. and Tans, P. P.: Estimating uncertainty of the WMO mole fraction scale for carbon dioxide in air, J. Geophys. Res. Atmospheres, 111(D8), D08S09, doi:10.1029/2005JD006003, 2006.

Zolot, A. M., Giorgetta, F. R., Baumann, E., Nicholson, J. W., Swann, W. C., Coddington, I. and Newbury, N. R.: Direct-comb molecular spectroscopy with accurate, resolved comb teeth over 43 THz, Opt. Lett., 37(4), 638–640, doi:10.1364/OL.37.000638, 2012.

Zolot, A. M., Giorgetta, F. R., Baumann, E., Swann, W. C., Coddington, I. and Newbury, N. R.: Broad-band frequency references in the near-infrared: Accurate dual comb spectroscopy of methane and acetylene, J. Quant. Spectrosc. Radiat. Transf., 118, 26–39, doi:10.1016/j.jqsrt.2012.11.024, 2013.

Atmos. Meas. Tech. Discuss., doi:10.5194/amt-2017-62, 2017
Manuscript under review for journal Atmos. Meas. Tech.
Discussion started: 14 March 2017

Atmospheric Measurement Techniques Discussions

	DCS A	DCS B
Design Details		
Comb 1 repetition rate (f_r)	~200 MHz	~204 MHz
Difference in repetition rate (Δf_r)	624 Hz	870 Hz
Spectral filtering	Before combining combs	After combining combs
Booster amplifier	Yes	No
Average power launched	4 mW	1.5 mW
Filtered spectral output	6376 to 6023 cm^{-1}	6359 to 6003 cm^{-1}
Telescope design	Home-built 3”-diameter off-axis telescope	Modified commercial 6”-diameter Ritchey-Chretien telescope
Retroreflector	2.5” HCC, 5 arc seconds	5” HCC, 5 arc seconds
Round-trip path length	1950.17 m	1963.67 m
Typical averaging time	32 s	28 s
Performance Metrics		
30-second precision	0.90 ppm CO_2, 9.6 ppb CH_4	2.15 ppm CO_2, 11.5 ppb CH_4
5-minute precision	0.24 ppm CO_2, 2.1 ppb CH_4	0.60 ppm CO_2, 3.2 ppb CH_4

578
579 **Table 1:** Specifications of the two DCS systems. HCC: hollow corner cube
580

Atmos. Meas. Tech. Discuss., doi:10.5194/amt-2017-62, 2017
Manuscript under review for journal Atmos. Meas. Tech.
Discussion started: 14 March 2017

Atmospheric Measurement Techniques Discussions

Systematic source [effect]	Effect on retrieved CO_2	Effect on retrieved CH_4	Effect on retrieved H_2O
Fitting procedure [initial guess, baseline polynomial order and window size]	0.07 ppm	1.4 ppb	4 ppm
Rf detection and processing [rf reflections, ADC nonlinearities]	0.16 ppm	0.34 ppb	1.0 ppm
Telescope system [Scattered light, polarization effects]	0.45 ppm	1.5 ppb	56 ppm
Spectral database [linestrengths in HITRAN 2008]	1-2%	10-20%	5-10%
Temperature path inhomogeneities [if <10 C across path]	0.024 ppm	0.36 ppb	3.52 ppm
Path-averaged temperature [for 0.5 C uncertainty]	0.64 ppm	2.9 ppb	8.6 ppm

Table 2: List of systematic uncertainties. See discussion in Section 3.2 and 3.4 for more details. Upper half of table: systematics due to hardware and software. Lower half of the table: systematics due to spectral model and temperature uncertainties.

Atmos. Meas. Tech. Discuss., doi:10.5194/amt-2017-62, 2017
Manuscript under review for journal Atmos. Meas. Tech.
Discussion started: 14 March 2017

Atmospheric Measurement Techniques Discussions

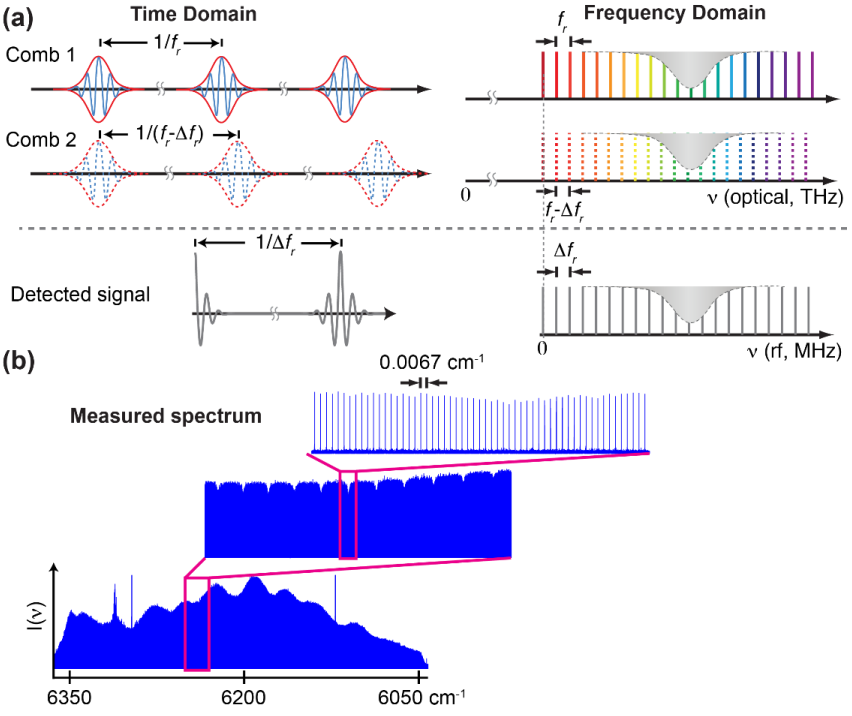

Figure 1. (a) Time and frequency domain overview of dual comb spectroscopy. Two frequency combs are phase-locked together with pulse repetition rates of f_r and f_r -Δf_r . Their detected heterodyne signal is a series of interferograms in the time domain, or equivalently a comb in the radio frequency (rf) domain. Provided the combs are sufficiently coherent and Nyquist sampling conditions are met, each rf comb tooth maps to a particular, known pair of optical frequency comb teeth (Coddington et al., 2008). As a result, the optical spectrum can be obtained from the magnitude of each rf comb tooth versus the average optical frequency of the relevant comb tooth pair. (b) Actual DCS spectrum acquired over 1.15 seconds for DCS A after transmission over 2-km air path. The overall shape is governed by the comb spectrum but there are narrow absorption dips present from atmospheric gases, as shown in the first expanded view. The second expanded view shows the fully resolved rf comb teeth with time-bandwidth limited widths. The highly resolved nature of these spectral elements translates to a negligible instrument lineshape, set by the narrow comb linewidths. The sample points are separated by 0.0067 cm^{-1} (or f_r =200 MHz). For long-term averaging, we implement coherent co-adding of interferograms that effectively measures the power at the individual rf comb teeth (Coddington et al., 2008)

Atmos. Meas. Tech. Discuss., doi:10.5194/amt-2017-62, 2017
Manuscript under review for journal Atmos. Meas. Tech.
Discussion started: 14 March 2017

Atmospheric Measurement Techniques Discussions
Open Access
EGU

602

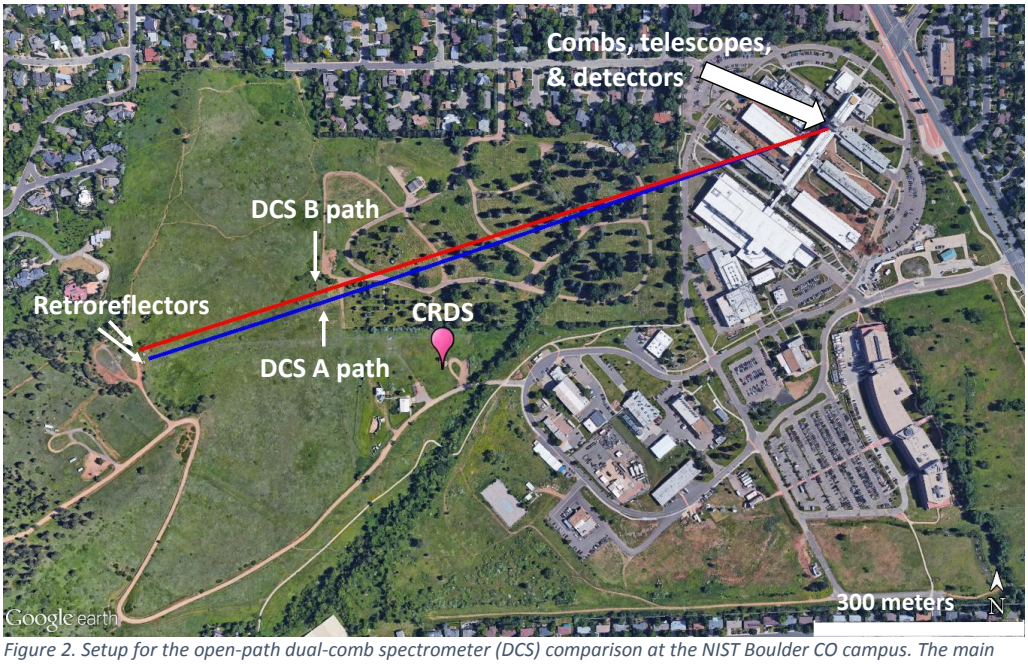

603
604 *Figure 2. Setup for the open-path dual-comb spectrometer (DCS) comparison at the NIST Boulder CO campus. The main*
605 *components for DCS A and DCS B are housed in a rooftop laboratory, including the frequency combs, telescope, receiver, and*
606 *processor. For each DCS, the combined comb light is launched from a telescope, travels ~1 km through the atmosphere to a*
607 *retroreflector, and returns to the telescope where it is collected, detected and processed. A separate cavity ringdown point*
608 *sensor (CRDS) is located nearby with an inlet on a 30-m tower that is located ~160 meters from the nearest point of the free-*
609 *space DCS paths.*

Atmos. Meas. Tech. Discuss., doi:10.5194/amt-2017-62, 2017
Manuscript under review for journal Atmos. Meas. Tech.
Discussion started: 14 March 2017

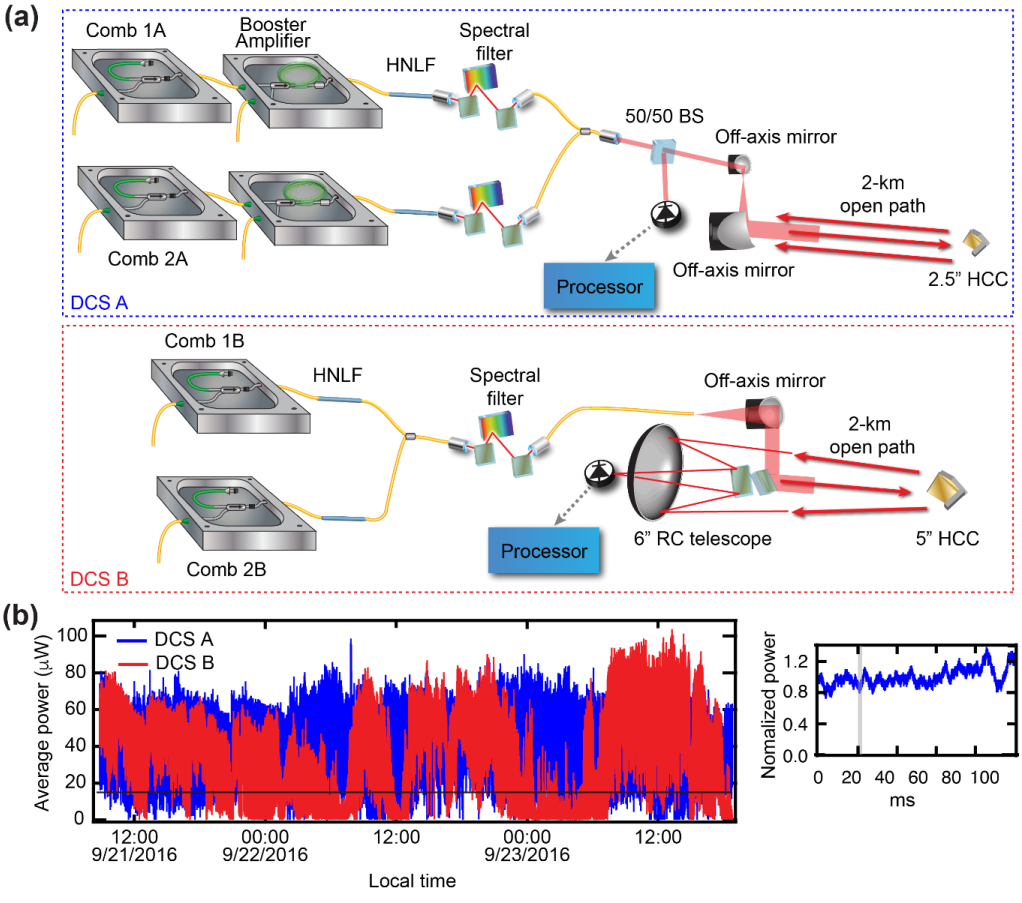

Figure 3. (a) Configuration of DCS A and DCS B, both of which are based on fully self-referenced fiber-laser frequency combs. See text and Table I for details. DCS A includes a booster amplifier for higher launched optical power than DCS B. (b) Average optical return power for DCS A (blue) and DCS B (red) measured at the detector over about 2.5 days. The horizontal black line shows the approximate minimum power for useable SNR (15 μW). Inset: The normalized power fluctuations for DCS A over 100 ms. The acquisition time for a single DCS spectrum is shown by the thickness of the vertical grey bar. RC: Ritchey-Chretien; HNLF: highly nonlinear fiber; HCC: hollow corner cube retroreflector; BS: beam splitter.

Atmos. Meas. Tech. Discuss., doi:10.5194/amt-2017-62, 2017
Manuscript under review for journal Atmos. Meas. Tech.
Discussion started: 14 March 2017

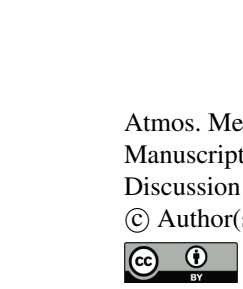

Atmospheric Measurement Techniques Discussions

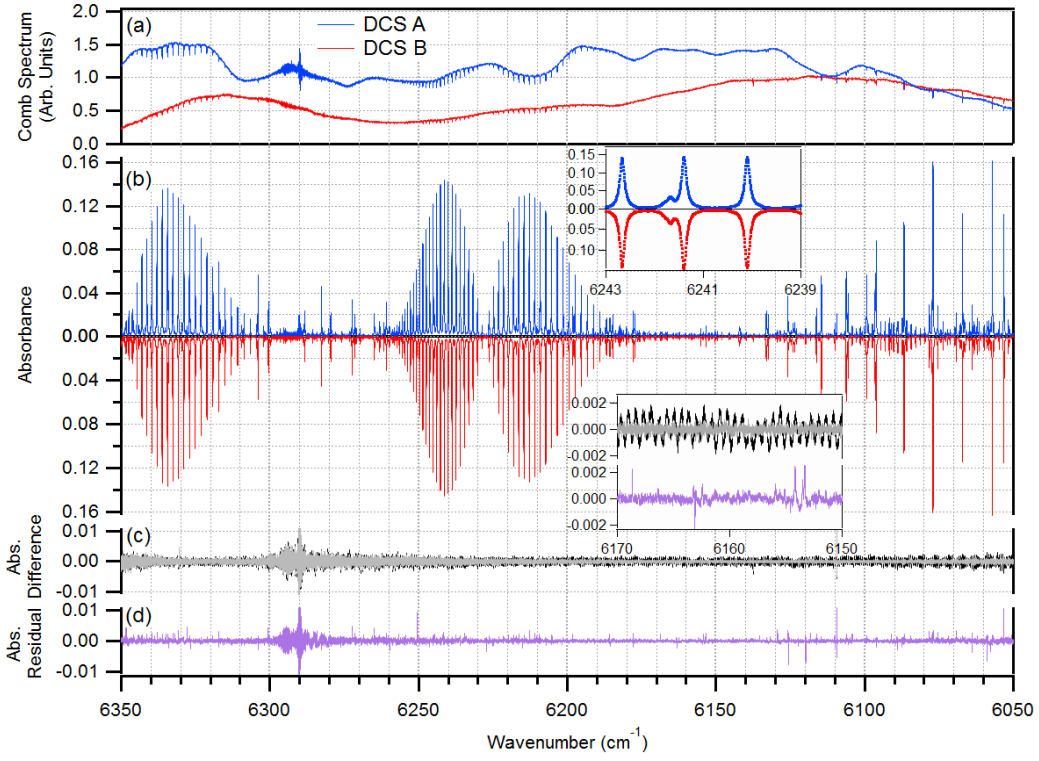

Figure 4. Raw spectra from DCS A (blue) and DCS B (red). (b) Corresponding baseline-corrected absorption spectra averaged for a three-hour period. The spectra overlap completely on this scale so the DCS A absorbance has been flipped about zero. Inset: expanded view of several CO_2 lines. (c) Difference between the absorption spectra from DCS A and DCS B. The difference is shown both before (black trace) and after (grey trace) removing an etalon structure and agree to better than 5×10^{-4} after the etalon is removed. Inset: Expanded view. (d) Residuals from a fit of the DCS A spectrum to HITRAN 2008. In general, the residuals are lower noise than the difference spectrum because of the higher signal-to-noise ratio of the DCS A than DCS B, but there are clear structures present near absorption lines due to imperfect line shapes of the spectral database.

Atmos. Meas. Tech. Discuss., doi:10.5194/amt-2017-62, 2017
Manuscript under review for journal Atmos. Meas. Tech.
Discussion started: 14 March 2017

Atmospheric Measurement Techniques Discussions

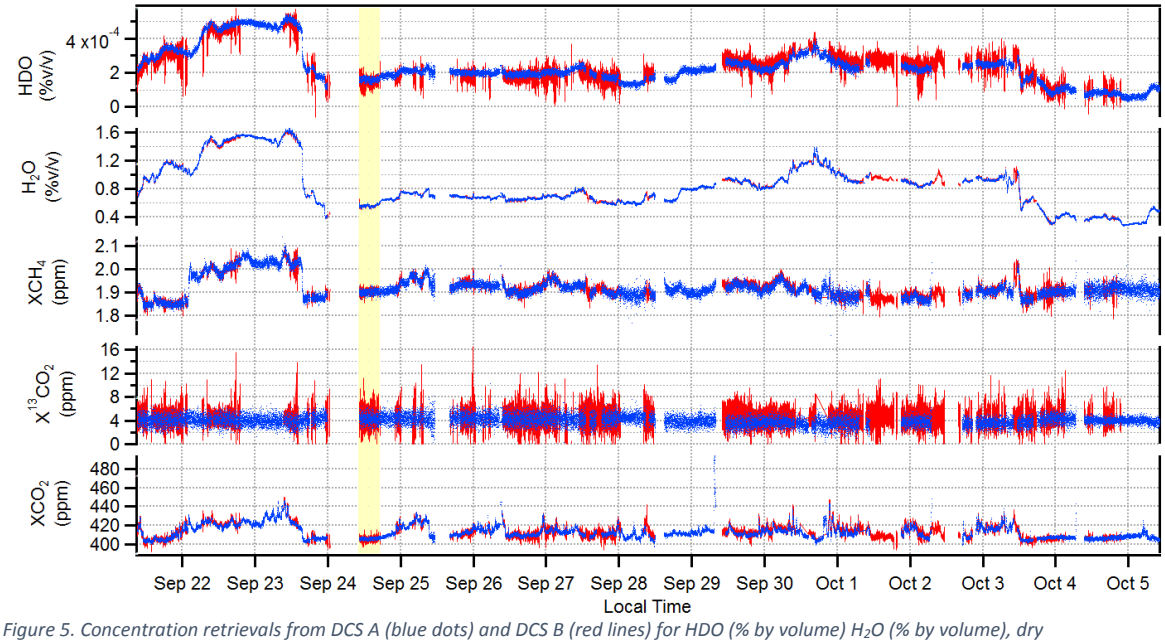

Figure 5. Concentration retrievals from DCS A (blue dots) and DCS B (red lines) for HDO (% by volume) H_2O (% by volume), dry CH_4, dry CO_2 and dry $^{13}CO_2$ over two weeks at 30-second intervals. Excellent agreement is observed between both systems for all species, though it is clear that over this path length $^{13}CO_2$ does not provide a strong enough signal to retrieve reliably. Highlighted section: 6-hour, well-mixed period over which Allan deviations (Figure 8) are calculated. Missing data is primarily due to telescope misalignment and less frequently, phase lock by one of the combs.

Atmos. Meas. Tech. Discuss., doi:10.5194/amt-2017-62, 2017
Manuscript under review for journal Atmos. Meas. Tech.
Discussion started: 14 March 2017

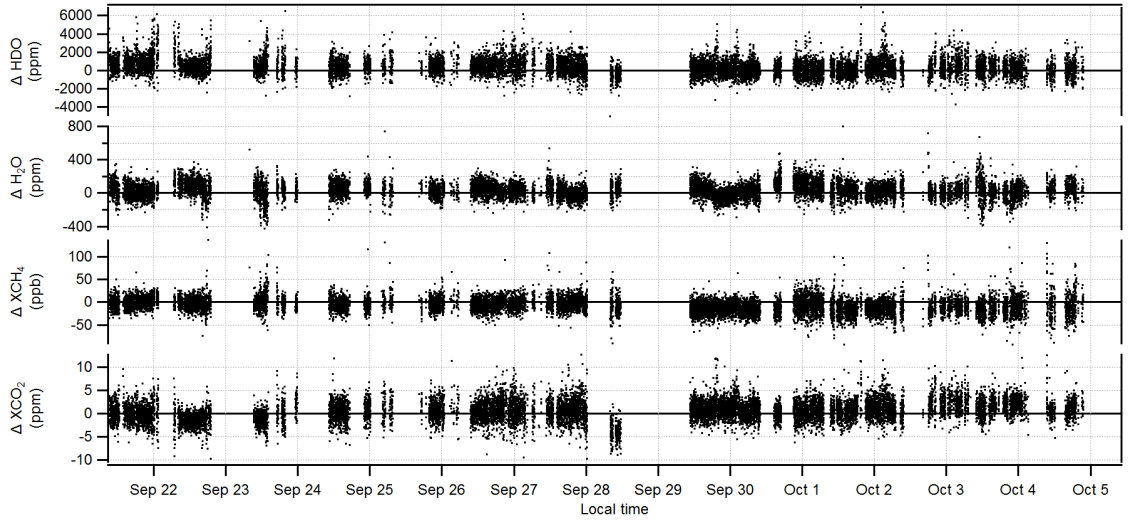

Figure 6. Time series of concentration differences, where difference is defined as DCS A - DCS B.

Atmos. Meas. Tech. Discuss., doi:10.5194/amt-2017-62, 2017
Manuscript under review for journal Atmos. Meas. Tech.
Discussion started: 14 March 2017

Atmospheric Measurement Techniques Discussions

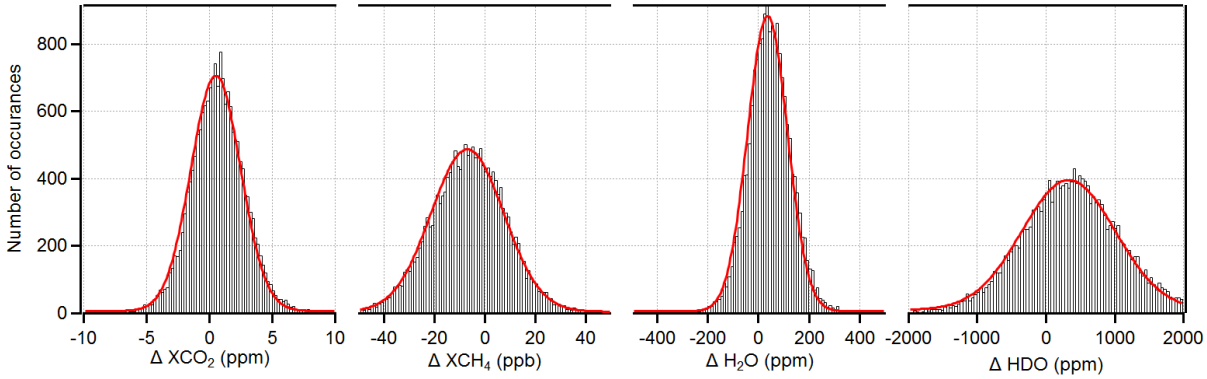

Figure 7. Statistical distributions of the differences between DCS A and DCS B for dry CO_2, dry CH_4, H_2O, and HDO from Fig. 6. Histograms are shown in black with a fit to Gaussian curves in red. These data are for ~30-second intervals; the widths are approximately halved if the data is averaged to 5-minute intervals.

Atmos. Meas. Tech. Discuss., doi:10.5194/amt-2017-62, 2017
Manuscript under review for journal Atmos. Meas. Tech.
Discussion started: 14 March 2017

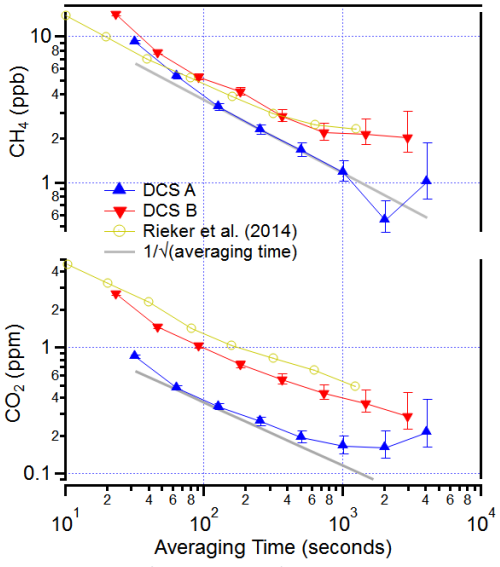

642
643 *Figure 8. Precision (Allan deviation) versus averaging time, τ, for CH_4 and CO_2 calculated for DCS A (blue) and DCS B (red) over a*
644 *2 km path for the time period highlighted in Figure 3. The previously-published precisions from Rieker et al. (2014) are also*
645 *shown (gold). The grey line illustrates the slope expected for white noise. For DCS A, at averaging times from 30s to 1000s, the*
646 *precision roughly follows* $\sim 40\ ppbv/\sqrt{\tau}$ *for CH4 and* $\sim 4\ ppmv/\sqrt{\tau}$ *for* CO_2 *(gray lines).*

Atmos. Meas. Tech. Discuss., doi:10.5194/amt-2017-62, 2017
Manuscript under review for journal Atmos. Meas. Tech.
Discussion started: 14 March 2017

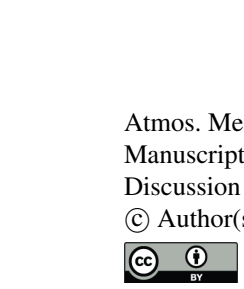

Atmospheric Measurement Techniques Discussions

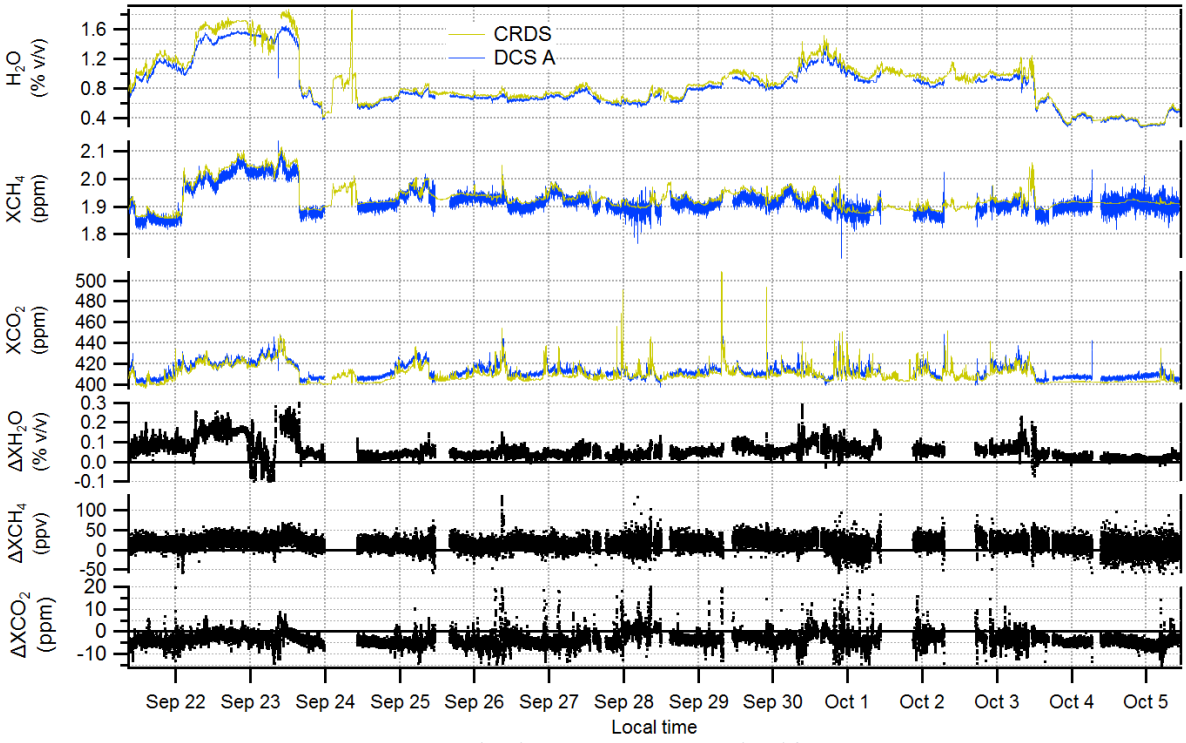

Figure 9. Comparison between the open-path DCS A data (blue) and the point CRDS data (gold) for H_2O, dry CH_4, and dry CO_2 at 32-second intervals over two weeks. The lower three panels directly plot the corresponding difference between the two.

Atmos. Meas. Tech. Discuss., doi:10.5194/amt-2017-62, 2017
Manuscript under review for journal Atmos. Meas. Tech.
Discussion started: 14 March 2017

Atmospheric Measurement Techniques Discussions

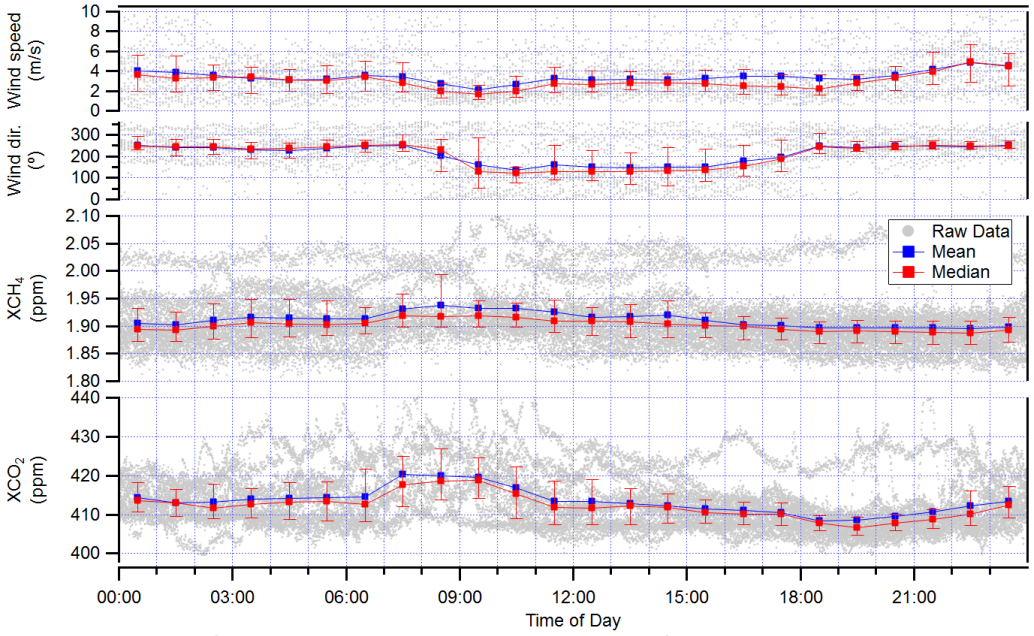

652
653 *Figure 10. Diurnal cycles for wind speed, wind direction, XCH_4, and XCO_2. Data from each day in Figure 5 is over-plotted in grey*
654 *along with the hourly mean (blue) and median (red) values. Uncertainty bars on the median values span the 75th quantile and*
655 *25th quantile.*

656

Atmos. Meas. Tech. Discuss., doi:10.5194/amt-2017-62, 2017
Manuscript under review for journal Atmos. Meas. Tech.
Discussion started: 14 March 2017

Atmospheric Measurement Techniques Discussions

Appendix A: Temperature studies

As described in Section 2.4, we extract the path-averaged temperature directly from a fit to the 30013 ← 00001 overtone band of CO_2. We perform this fit on 5-minute averages, rather than 32-second averages, under the assumption the temperature changes are still slow at that timescale. This path-averaged temperature is then used in a subsequent fit over the full spectral region to extract the column densities, and finally the mole fractions. We use a common temperature (from DCS A fit) to analyze both data sets in order to separate out instrument effects from the temperature, but the fitted temperatures between instruments show less than 0.25 °C bias.

Figure A1 compares this fitted path-averaged temperature from DCS A to three point sensors, two of which are located on the rooftop near the telescope launch point and one that is located ~ 2.2 km away at an altitude ~200 m above the overall open path. As shown in Figure A1, the two rooftop temperature sensors located near the telescope agree well with each other, but do not agree with the fitted path-averaged temperature. Moreover, that disagreement has a distinct diurnal character, supporting the argument it arises from a real temperature gradient. In contrast, the path-averaged temperature does often agree well with the temperature measured by the third temperature point sensor located at similar or higher altitude as the open path on the NCAR Mesa building (ftp://ftp.eol.ucar.edu/pub/archive/weather/mesa/). These data indicate that the point sensor located at the telescope site is not a good proxy for the path-averaged temperature; instead, the fitted path-averaged temperature should be used for the concentration fits because of temperature gradients. Note that the temperature gradients themselves do not lead to appreciable errors in the retrieved mole fractions if the correct path-averaged temperature is used (see Table 2 and Section 3.4).

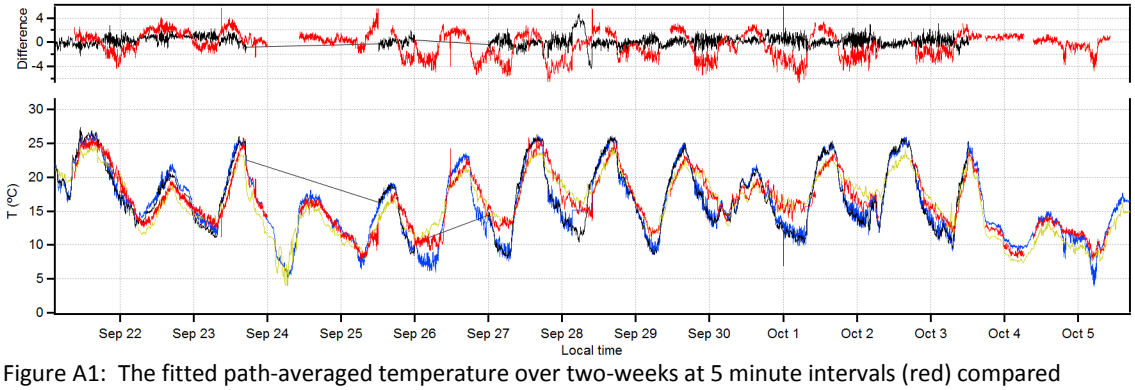

Figure A1: The fitted path-averaged temperature over two-weeks at 5 minute intervals (red) compared to the measured air temperature from a roof-top anemometer located near the telescope (blue), a second thermistor temperature sensor also located on the roof but 100-m distant (black), and a third rooftop temperature ~2.2 km distant at the NCAR Mesa facility (gold). Top panel: The difference between the two rooftop temperature (black) agree to within 1°C, but the difference between these rooftop sensors and fitted path-averaged temperature (red) shows larger 2-4°C diurnal differences, indicating it is not sufficient to measure the temperature at one “end point” of the open path. In fact, the path-averaged temperature agrees better with the more distant, but higher elevation temperature sensor located at the NCAR Mesa facility.